JOURNAL OF AIRCRAFT
Vol. 47, No. 4, July–August 2010

Computation of Flow over a High-Performance Parafoil Canopy

Mohammad A. Mohammadi* and Hamid Johari†
California State University, Northridge, California 91330

DOI: 10.2514/1.47363

The incompressible Navier–Stokes equations together with the one equation Spalart–Allmaras turbulence model were solved using a finite volume flow solver to examine the flowfield and forces on the central cross section of a high-performance parafoil canopy. The parafoil surfaces were assumed to be impermeable, rigid, and smooth. The flowfield consists of a vortex inside the parafoil cell opening, which effectively closes off the opening and diverts the flow around the leading edge. The flow about the parafoil experiences a rather bluff leading edge, in contrast to the smooth leading of the baseline airfoil. A separation bubble exists on the lip of the parafoil lower surface. The lift coefficient of the parafoil section increases linearly with the angle of attack up to 8.5 degrees and the parafoil lift-curve slope is about 8% smaller than the same for the baseline airfoil. The cell opening has a major effect on the drag before stall; the parafoil drag is at least twice the baseline airfoil drag. The minimum drag of the parafoil section occurs over the angle-of-attack range of 2.5–7 degrees.

I. Introduction

THE success of the Joint Precision Airdrop System (JPADS) program [1,2] has been achieved by a family of high-performance ram-air type parachutes. These parachute systems allow for high-altitude deployment, large offset ranges, demanding accuracy, and soft-landing capabilities. One of the key drivers of the technology behind high-performance ram-air parachutes, also known as parafoils, is the aerodynamics of the canopy. Ram-air parachute canopies have surface areas ranging from 120 ft^2 for sport jumping applications to 9000 ft^2 for the MegaFly and 10,400 ft^2 for the Gigafly canopies. The majority of current knowledge and design rules for ram-air parachutes are contained in the Heinrich Parachute Systems Technology Short Course by Lingard [3]. Not only are the basic wing lift and drag relationships discussed, but also the practical ranges of various parameters are provided for preliminary design purposes.

Although wind tunnel studies of ram-air parachutes have been carried out in the past [4–7], computational studies of parafoils have focused on rigid models [7,8]. This is perhaps due to the computational challenges associated with the modeling of fluid–structure interaction systems. Parafoils have typically much higher drag when compared with a rigid wing of the same geometry without the opening at the leading edge. Computations of flow around parafoil sections with a low-speed airfoil profile LS(1)-0417 have been carried out by Ross [8] and more recently by Balaji et al. [9]. Two- and three-dimensional potential flow computations of Ross [8] show that the leading-edge cut at the cell opening has a significant effect on the performance, and the lift-to-drag ratio can be increased by reducing the cell opening and modifying the opening position with respect to the airfoil stagnation point. The two-dimensional Reynolds-averaged Navier–Stokes (RANS) computations of Balaji et al. [9] using a finite element formulation and the Baldwin–Lomax turbulence model revealed that at an angle of attack of $\alpha = 7.5$ deg the glide ratio can be increased by a well-placed cut at the airfoil leading edge. Mittal et al. [10] using the same computational approach as Balaji et al. [9] found that the cut also affects the performance of a Clark-Y based parafoil section at $\alpha = 7.5$ deg. Three-dimensional Navier–Stokes computations of the flow around a parafoil model with a Clark-Y cross section and a closed, rounded leading edge have been carried out by Kalro et al. [11,12]. The model in these studies did not have an open inlet, and the critical flow features associated with the parafoil opening are missing.

It is important to denote that a parafoil canopy differs from a rigid wing, even apart from the opening at the leading edge. A parafoil canopy is typically divided into sections called "cells" in the spanwise direction. Fabric having the airfoil cross section joins the adjacent cells. Internal air pressure balloons out the external surface of the canopy resulting in a ribbed appearance. In some canopy designs, the fabric joining adjacent cells has openings that allow the air pressure to equilibrate between neighboring cells. Moreover, the extent of the opening may not be the same across the canopy. Such features as well as the open inlet at the leading edge create differences between the flow over a parafoil canopy and a rigid wing having a similar cross section. However, we believe that the flow features over a section of the canopy with the open leading edge warrant a detailed study to allow a better understanding of the observed characteristics.

The present computational study examines the flow around the center section of a modern high-performance parafoil canopy. The aerodynamic performance of the canopy, which is assumed to be rigid, is computed at angles of attack ranging from $-3.5\ \mathrm{deg} \le \alpha \le 11.5$ deg and at three operationally relevant velocities. The lift and drag of the parafoil with the open leading edge is compared against the baseline airfoil from which the parafoil geometry was derived. The flowfield details reveal the fundamental reason for the increased drag associated with parafoils. The numerical scheme used is described in Sec. II and the mesh sensitivity study in Sec. III; the results are presented in Sec. IV. The findings are summarized in Sec. V.

II. Numerical Methodology

The steady-state RANS equations under the constant property, incompressible flow assumption were solved over a rectangular domain containing the airfoil/parafoil cross section. The one equation Spalart–Allmaras turbulence model [13] that is appropriate for aerodynamic flows at higher Reynolds numbers was used to account for the turbulent stresses. The equations were solved by the well-established finite volume flow solver FLUENT. The no-slip boundary condition was applied to the interior and exterior surfaces of the parafoil sections and the baseline airfoil surface. The parafoil fabric was assumed to be impermeable and rigid. The boundary conditions on the computational domain consisted of uniform velocity (freestream value) at the inflow and vanishing viscous stress

---

Presented as Paper 2009-2979 at the 20th AIAA Aerodynamic Decelerator Systems Technology Conference and Seminar, Seattle, WA, 4–7 May 2009; received 25 September 2009; revision received 2 February 2010; accepted for publication 2 February 2010.

*Graduate Student, Department of Mechanical Engineering, 18111 Nordhoff Street, Mail Stop 8348.

†Professor, Department of Mechanical Engineering, 18111 Nordhoff Street, Mail Stop 8348. Associate Fellow AIAA.

(traction-free) at the outflow boundary. The transverse velocity component on the upper and lower boundaries was set to zero (free slip), which makes these boundaries into streamlines.

The surface geometry of the baseline airfoil and the parafoil section were imported into Gambit, the mesh generator software. The upper and lower exterior surfaces of the parafoil section were discretized by a rectangular boundary-layer-type structured mesh to accurately and efficiently capture the boundary-layer characteristics. An internal boundary separated the parafoil interior from the external region across the parafoil cell opening. The parafoil interior was discretized by an unstructured triangular mesh. Outside the boundary-layer-type mesh on the parafoil surfaces, an unstructured triangular mesh was used to discretized the rest of the domain.

For each angle of attack, the geometry of the parafoil section and the baseline airfoil were defined with respect to the freestream in the computational domain before discretization. Then, the domain was discretized with the same mesh resolution and growth rate. Even though the number of cells and nodes changes with each angle of attack, the mesh resolution and density were nearly the same for all the cases examined. The computations were performed on a Windows workstation with 4 GB of memory. A sufficient number of iterations was carried out for each case such that the normalized residuals had decreased by 4 orders of magnitude.

III. Mesh and Domain Sensitivity

To assess the effects of the computational domain and the mesh parameters on the flowfield and the resulting forces, a standard Clark-Y airfoil at a Reynolds number of 500,000 was chosen as a test case. A detailed experimental data set [14] exists for this airfoil at the chosen Reynolds number. The time averaged lift and drag coefficients of the Clark-Y airfoil at an angle of attack of $\alpha = 6\,\mathrm{deg}$ are 0.985 and 0.0205, respectively, with an uncertainty of $\pm 2.5\%$. The flowfield was computed at $\alpha = 6\,\mathrm{deg}$ for various domain extents and mesh characteristics, and the resulting lift and drag coefficients were compared against the experimental data. The airfoil at $\alpha = 6\,\mathrm{deg}$ along with a sample mesh is shown in Fig. 1.

Four domain sizes of 30×20, 23×16, 16×10, and 7×4 chord lengths were considered. The first dimension refers to the domain extent in the freestream direction and the second dimension to the transverse direction. The airfoil was placed halfway between the top and bottom boundaries, and five chord lengths ($5c$) from the inflow for the three largest domains. For the smallest domain, the airfoil leading edge was only two chord lengths ($2c$) from the inflow. The computed lift and drag values showed that for all domains, except the 7×4 case, the computed values are within the uncertainty of the experimental values. The drag coefficient was more sensitive to the changes in the domain size than the lift coefficient. For the smallest domain of 7×4 chord lengths, the computed drag was nearly 9% greater and the lift was nearly 3% greater than the corresponding experimental values. Thus, the $16c \times 10c$ domain was deemed sufficiently large to perform the computational study.

To assess the mesh resolution effects, the rectangular-cell dimension on the airfoil surface, the height of the first rectangular cell above the surface, as well as the growth rate of the structured rectangular mesh and the unstructured triangular mesh were varied systematically for the Clark-Y airfoil at $\alpha = 6\,\mathrm{deg}$. The flow was computed for each case and the resulting lift and drag values were compared against the experimental data. The computed lift coefficients were generally within the uncertainty of the experimental value; however, the drag coefficient was a better indicator of the fidelity of the computational mesh characteristics. The mesh sensitivity analysis resulted in the following characteristics: 3 mm surface dimension, 2 mm first cell transverse dimension, growth factor of 1.02 for the structured rectangular cells and 1.03 for the unstructured triangular cells.

To estimate the uncertainty due to the discretization in the computations, the ASME recommended procedure [15], which is based on the Richardson extrapolation, was followed. Three significantly different sets of mesh for the Clark-Y airfoil at $\alpha = 6\,\mathrm{deg}$ were created, and the lift and drag coefficients were chosen as the key parameters. The mesh refinement factor between the mesh pairs was 5 and 1.4. The calculated apparent order of the method resulted in values of 3.9 for the drag and 9.8 for the lift. The approximate relative error was 2.95 and 0.04% for the drag and lift, respectively. The extrapolated relative error was less than 0.01% for the drag and lift. The fine-grid convergence index was 0.007 and 0.06% for the drag and lift, respectively. Hence, a relative error of less than 3% and a fine-grid convergence index of less than 0.1% are reported for the computations carried out in this study.

Based on the results of the Clark-Y study, all the computations of the baseline airfoil and the parafoil section presented henceforth were carried out in a domain of $16c$ in the flow direction, $5c$ upstream and $11c$ downstream of the leading edge, and $10c$ in the transverse direction. The baseline airfoil surface was covered by a boundary-layer-type mesh and an unstructured triangular mesh elsewhere. A schematic of the computational domain and the boundary conditions are shown in Fig. 2.

For the parafoil section, an unstructured triangular mesh covered the computational domain except the area immediately above the upper surface and below the lower surface where a boundary-layer-type mesh was used. The mesh in each case had the characteristics stated in the previous paragraphs with the following specifications: 5×10^{-4} chord length axial dimension of the surface rectangular cell, 3.5×10^{-4} chord length transverse dimension of the first cell, growth factor of 1.02 for the structured rectangular cells, and 1.03 for the unstructured triangular cells.

IV. Results

The flowfield about the baseline airfoil as well as the parafoil cross section and the associated forces and moments are discussed in this section. The angle of attack was varied over the range of $-3.5\,\mathrm{deg} \leq \alpha \leq 11.5\,\mathrm{deg}$, and three freestream velocities of $V_\infty = 9.4$, 15.0, and 20.9 m/s were examined. For the parafoil section, the angle of attack is defined by the baseline airfoil angle, i.e., the orientation that closely matches with the baseline airfoil at that angle of attack. The Reynolds number based on the freestream velocity and the mean chord length ranged from 3.0–6.6 million. These freestream velocities correspond to the values along the flight

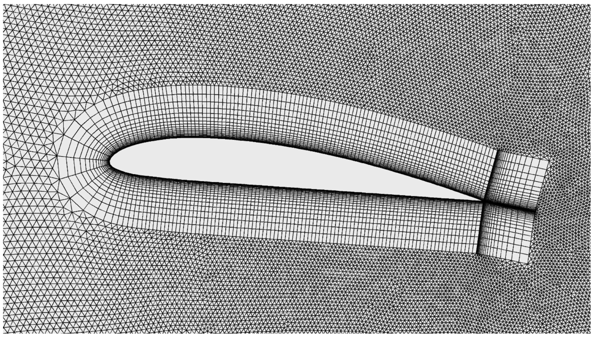

Fig. 1 Computational mesh for the Clark-Y airfoil at $\alpha = 6\,\mathrm{deg}$.

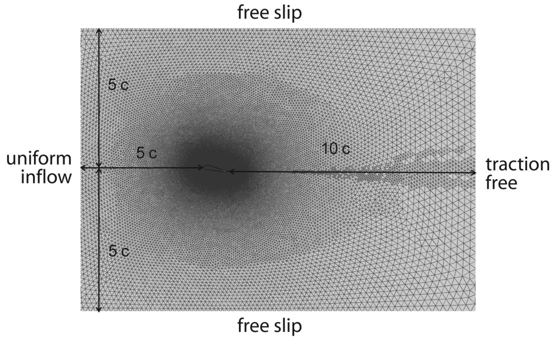

Fig. 2 Schematic of the computational domain and the boundary conditions used.

path for a range of the ram-air parachute loadings. Flow field data are presented in terms of the pressure coefficient, velocity magnitude, streamlines, and vorticity contours. The lift, drag, and moment coefficients are normalized by the freestream dynamic pressure and the chord length. For the parafoil section, the chord length refers to the distance from the leading edge on the upper surface to the trailing edge.

A. Baseline Airfoil

The baseline airfoil has a thickness ratio of 15.5% and is slightly reflexed. The computational mesh around this airfoil had 550,822 cells with 446,437 nodes. Contours of pressure coefficient around the airfoil at an angle of attack of $\alpha = 7$ deg is shown in Fig. 3 at a freestream velocity of $V_\infty = 20.9$ m/s. This angle of attack was chosen since it results in the highest lift-to-drag ratio over the range studied. As expected, there is a stagnation region near the leading edge and a low-pressure region over the suction side of the airfoil. The minimum pressure coefficient on the airfoil was -2.58. Pressure recovers smoothly from the minimum value toward the trailing edge of the airfoil.

The velocity magnitude contours for the same conditions as in Fig. 3 are presented in Fig. 4. The flow accelerates from the stagnation point near the leading edge to the top of the airfoil; then a thickening boundary layer is clearly visible on the suction side. The flow is fully attached at this angle of attack. This is further verified by the streamline pattern shown in Fig. 5. No flow reversal is evident on the airfoil at the $\alpha = 7$ deg angle of attack. The extent of the boundary layer becomes evident in the vorticity contours plotted in Fig. 6. The boundary layer on the suction side is about twice as thick as that on the pressure side.

The airfoil lift coefficient, C_l, is shown in Fig. 7 as a function of the angle of attack for the three freestream velocities. The airfoil lift increases linearly from $\alpha = -3.5$ to 8.5 deg, and the average lift-curve slope is 0.108/deg. The zero-lift angle of attack is $\alpha_{zl} = -1$ deg. The lift coefficient is nearly independent of the freestream velocity for the three values studied, implying that the flow is nearly Reynolds-number-independent in this range. The only exception is at $\alpha = 11.5$ deg, where the linear increase of lift with angle of attack has ceased. The drag coefficient, C_d, shown in Fig. 8 rises very slowly from the minimum value until $\alpha \approx 7$ deg, beyond this angle drag rises rapidly. Even though no experimental data were available for this airfoil for direct comparison, the computed lift and drag characteristics are typical for this type of airfoil at Reynolds numbers of a few million.

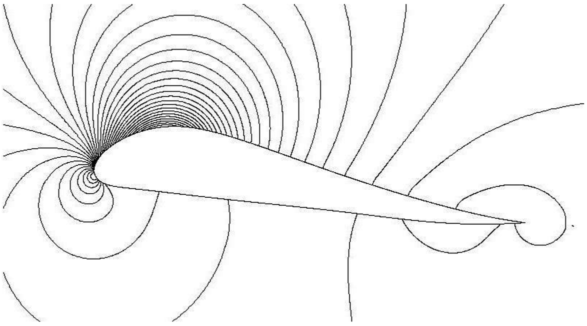

Fig. 3 Pressure contours about the baseline airfoil at $\alpha = 7$ deg. The minimum contour value is $C_p = -2.5$ and the maximum is 1.0 with a step of 0.14.

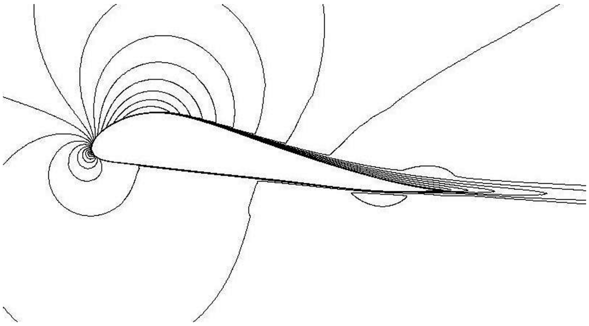

Fig. 4 Velocity magnitude contours about the baseline airfoil at $\alpha = 7$ deg. The minimum contour value is 0 and the maximum is 38.6 m/s with a step of 1.9.

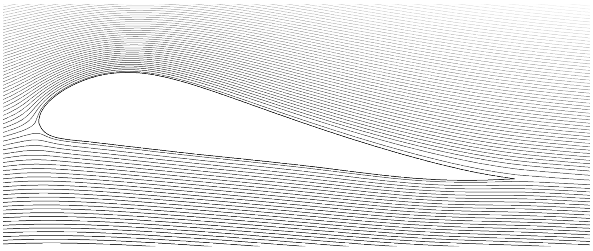

Fig. 5 Streamlines around the baseline airfoil at $\alpha = 7$ deg.

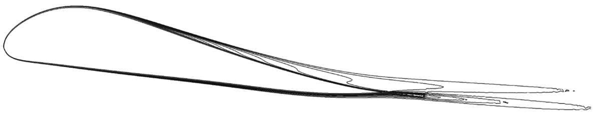

Fig. 6 Vorticity contours of the baseline airfoil at $\alpha = 7$ deg.

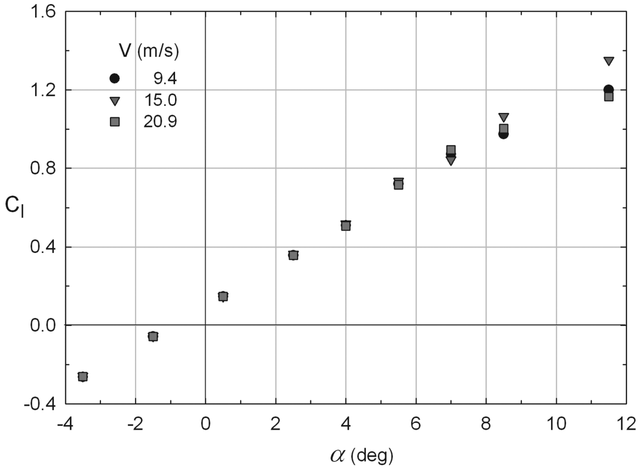

Fig. 7 Lift coefficient of the baseline airfoil at three different freestream velocities.

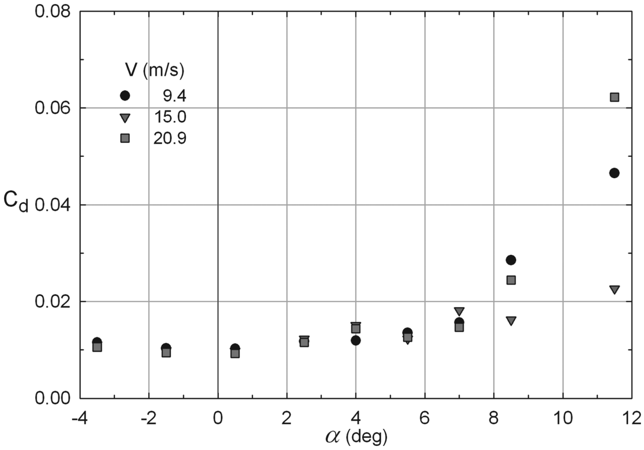

Fig. 8 Drag coefficient of the baseline airfoil at three different freestream velocities.

B. Parafoil

The computational mesh used for the parafoil section at an angle of attack of $\alpha = 7$ deg is shown in Fig. 9; the close-up image reveals the mesh near the leading edge of the parafoil section. The parafoil section inlet is partially covered (see Figs. 9 and 10), and the length of the lip is approximately 2.6% of the chord length. The mesh in Fig. 9 has 508,705 cells and 420,595 nodes. The interior unstructured triangular mesh interfaced with the exterior unstructured mesh at the cell opening. A feature in FLUENT allows dynamic adjustment of mesh density according to the flow gradients. This feature was used for the parafoil computations. The dynamic mesh density adjustment revealed that the flow gradients are quite weak inside the parafoil section, especially toward the trailing edge. On the other hand, the very high mesh density around the cell opening denotes large flow gradients in this region. The minimum boundary-layer-type cell dimension on the exterior surfaces of the parafoil is less than 0.04% of the chord length indicating adequate resolution.

The pressure field around the parafoil section at an angle of attack of $\alpha = 7$ deg and freestream velocity of $V_\infty = 20.9$ m/s is shown in Fig. 10. There is a high pressure region on the upper lip representing the stagnation point there. The pressure within the parafoil is nearly uniform and equal to the stagnation value except in a circular region just behind the upper leading edge, which has a lower pressure. There are also low-pressure regions on the top exterior surface, as expected, as well as beneath the lower leading edge. This low-pressure region is surprising as the lower exterior surface is typically the higher pressure side. Other than the anticipated differences at the opening of the parafoil and the unexpected low-pressure region on the lower (pressure) side, the pressure field on the parafoil is similar to that of the baseline airfoil (see Fig. 3).

The pressure coefficient C_p on the exterior surfaces of the parafoil as well as the baseline airfoil are shown in Fig. 11 for an angle of attack of $\alpha = 7$ deg and freestream velocity of $V_\infty = 20.9$ m/s. Pressure decreases rapidly from the stagnation point on the upper lip of the parafoil section due to the flow turning around the upper corner. There is a local recovery before C_p experiences its minimum value of -2.52 on the upper surface. Subsequently, the pressure C_p recovers toward the trailing edge on the upper surface. This C_p value is the same as the minimum C_p on the baseline airfoil, and it appears slightly forward of the minimum on the baseline airfoil.

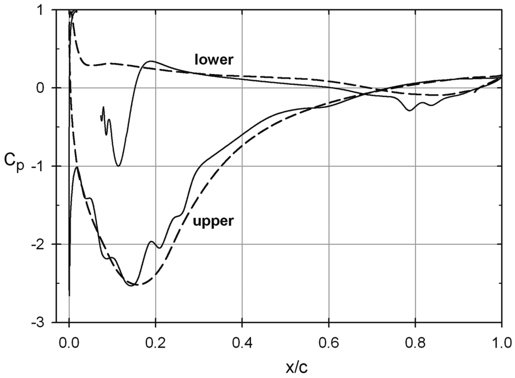

Fig. 11 Pressure coefficient on the upper and lower exterior surfaces of the parafoil canopy (solid curves) and on the baseline airfoil (dashed curve) at $\alpha = 7$ deg.

The pressure coefficient distribution on the lower surface of the parafoil indicates that there is a loss of pressure ($C_p = -1$) near the leading edge, due to flow separation. Then, C_p recovers to a positive value before another region of negative C_p near the trailing edge. The plot in Fig. 11 also shows that the lift is generated only over the first ~70% of the parafoil surface. The pressure coefficient for the baseline airfoil is very similar to that of the parafoil with the exception of a higher C_p value over the first part of lower surface where the parafoil has a separation bubble. The C_p for the baseline and the parafoil are identical after the halfway point of the chord length. The nearly identical C_p distributions of the baseline airfoil and the parafoil section indicate that the effects of the open inlet are confined to the leading-edge region.

The velocity magnitude about the parafoil section at an angle of attack of $\alpha = 7$ deg and freestream velocity of $V_\infty = 20.9$ m/s is shown in Fig. 12. The velocity magnitude data reveal that the highest velocities are encountered on the top of parafoil (at the

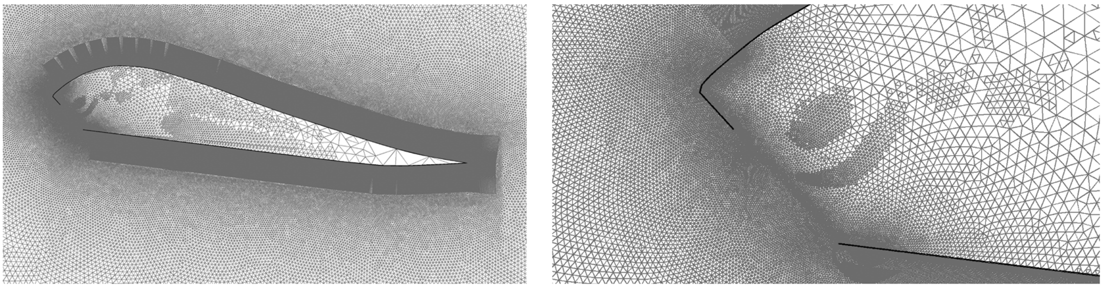

Fig. 9 Computational mesh used for the parafoil at $\alpha = 7$ deg.

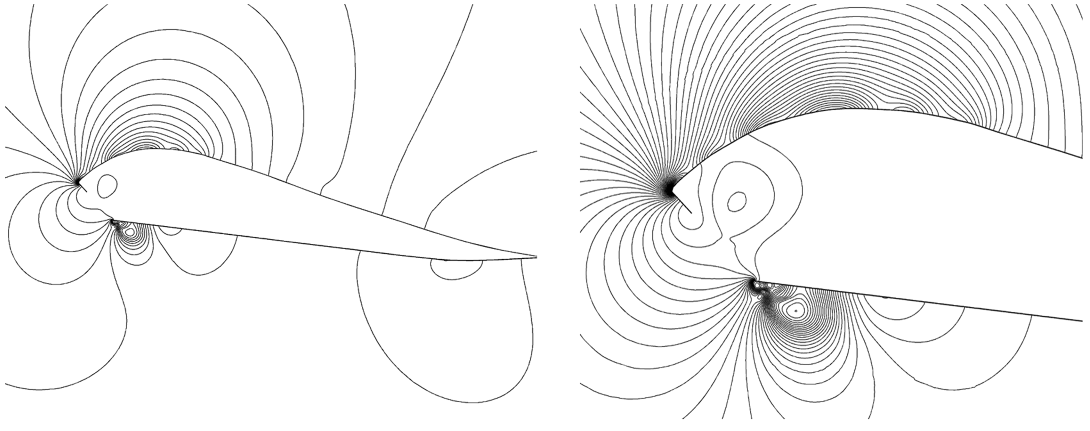

Fig. 10 Pressure contours about the parafoil section at $\alpha = 7$ deg. The minimum contour value is $C_p = -2.5$ and the maximum is 1.0.

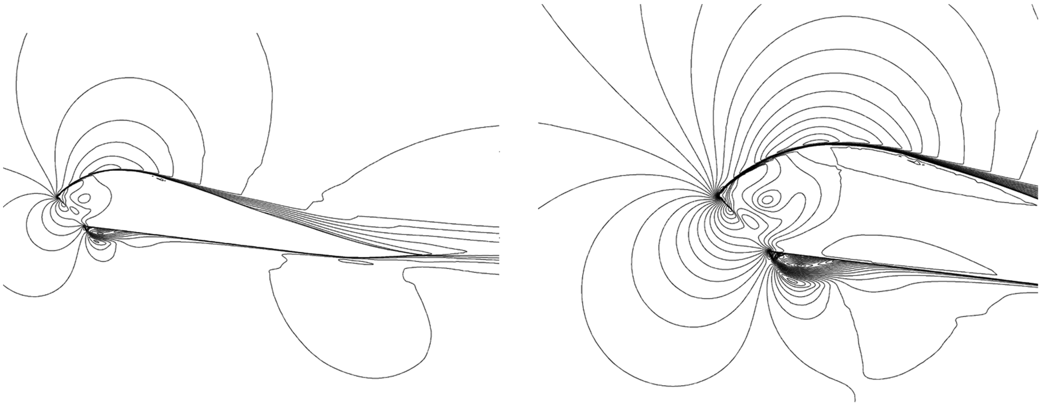

Fig. 12 Velocity magnitude contours about the parafoil at $\alpha = 7$ deg. The minimum contour value is 0 and the maximum is 38.9.

suction peak) as the flow accelerates, and a thick boundary layer appears as the flow decelerates toward the trailing edge. There is also a high velocity region just below the lower leading edge revealing a separation bubble. Within the parafoil, there is a circular low velocity region near the cell opening, followed by an expanding stagnant fluid indicated by the lack of contours. Essentially, the fluid motion ceases beyond the halfway point within the parafoil. The stagnation point at the leading edge is near the tip of the upper lip. Comparing the contours in Fig. 12 with those of the baseline airfoil in Fig. 4 reveals a thicker boundary layer on the upper (suction) surface and the separation bubble on the lower surface of the parafoil. Both features are expected to degrade the performance of the parafoil compared with the baseline airfoil.

The streamlines around the parafoil section at $\alpha = 7$ deg and $V_\infty = 20.9$ m/s are shown in Fig. 13. As revealed in Fig. 12, the stagnation point at the leading edge is on the tip of the upper surface lip. Streamlines above the stagnation point curve upwards and eventually accelerate over the top exterior surface. Streamlines below the stagnation point follow the cell opening to the lower lip. There, the flow has to turn sharply, thus creating a separation bubble. This separation bubble is the cause of the low pressure on the exterior of the lower surface observed in the close-up image of Fig. 10 and the negative C_p values near the leading edge of the lower surface. The flow reattaches further downstream due to the favorable pressure gradient on the lower surface; a thin boundary layer forms following the reattachment. The streamlines also reveal a vortex rotating counter clockwise just inside the cell opening. This vortex corresponds to the low velocity circular region in Fig. 12 at the same location. This vortex in effect blocks off the cell opening. A weaker, clockwise, secondary vortex also exists inside the parafoil. Streamlines at other angles of attack reveal a similar pattern in which a vortex is present just inside the parafoil opening and a separation bubble exists on the exterior of the lower leading edge. The vortex essentially closes off the cell opening and creates a bluff leading edge. The exterior flow does not penetrate the cell opening in these steady-state computations of the rigid parafoil section.

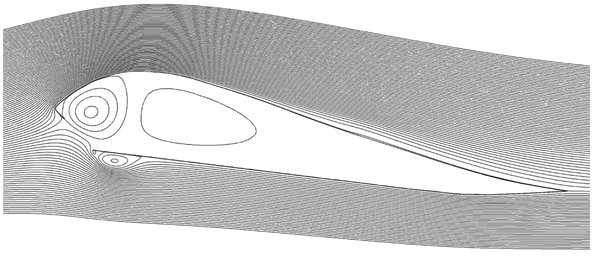

Fig. 13 Streamlines about the parafoil at $\alpha = 7$ deg.

Rotational flow around the parafoil section at $\alpha = 7$ deg and $V_\infty = 20.9$ m/s is indicated by the vorticity contours in Fig. 14. These contours clearly show the interior vortex near the cell opening as well as the separation bubble on the lower surface. The flow reattachment and the boundary-layer formation on the lower surface are evident in Fig. 14. The thickening boundary layer on the upper surface is also visualized in this figure. In corroboration with the velocity magnitude contours shown in Fig. 12, the lack of vorticity contours inside the parafoil and away from the opening indicates quiescent air. The vorticity contours further reveal a shear layer along the cell opening.

The computed lift coefficient is plotted in Fig. 15 for the three freestream velocities. The lift coefficient is nearly independent of the freestream velocity and Reynolds number up to $\alpha = 8.5$ deg. Beyond this angle of attack, the parafoil section at $V_\infty = 9.4$ m/s is stalled. On the other hand, the other two freestream values do not show a decreasing lift coefficient. The C_l increases linearly with the angle of attack for all three velocities. A best-fit line to all three data sets in Fig. 15 results in a lift-curve slope of 0.099/deg, and a zero-lift angle of attack of $\alpha_{\mathrm{zl}} = -0.8$ deg. This lift-curve slope is 8% less than the same for the baseline airfoil, and 10% less than the thin airfoil theoretical value.

The computed drag coefficient of the parafoil section is presented in Fig. 16. Contrary to the lift coefficient, the drag coefficient appears to be Reynolds-number-dependent for the majority of the angles of attack values examined. The solid line in Fig. 16 represents the average drag coefficient at each angle of attack. The lowest average drag coefficient exits over the $2.5\,\mathrm{deg} \le \alpha \le 7\,\mathrm{deg}$ range; drag values increase for angles of attack outside this range. Drag rises very rapidly for $\alpha > 8.5$ deg as the flow separation extends over the upper surface of the parafoil. For the $V_\infty = 9.4$ m/s case, drag coefficient becomes over 3 times greater than the lowest drag value as the parafoil stalls at $\alpha = 11.5$ deg. There is large scatter in the drag data at

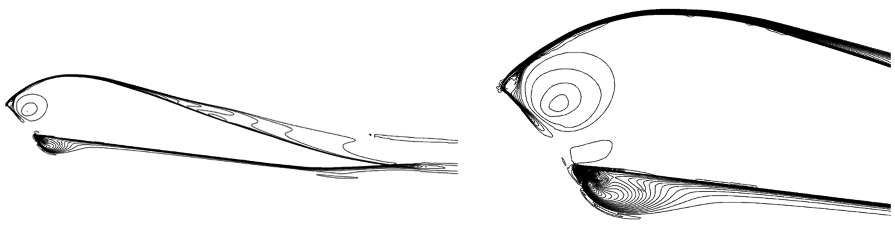

Fig. 14 Vorticity contours around the parafoil at $\alpha = 7$ deg.

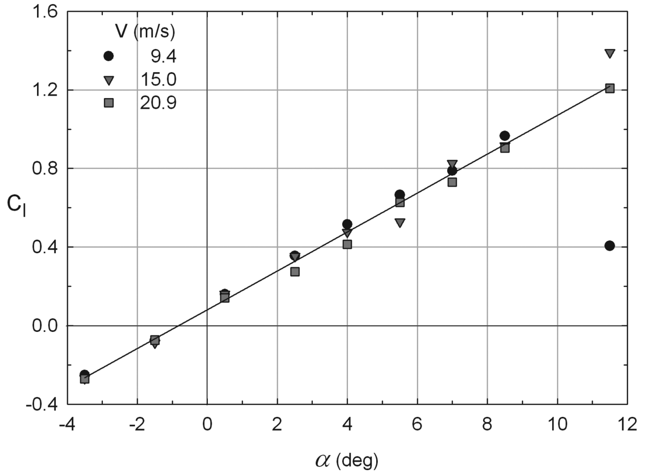

Fig. 15 Lift coefficient of the parafoil section at different freestream velocities. The best linear fit to the entire data set is indicated by the line.

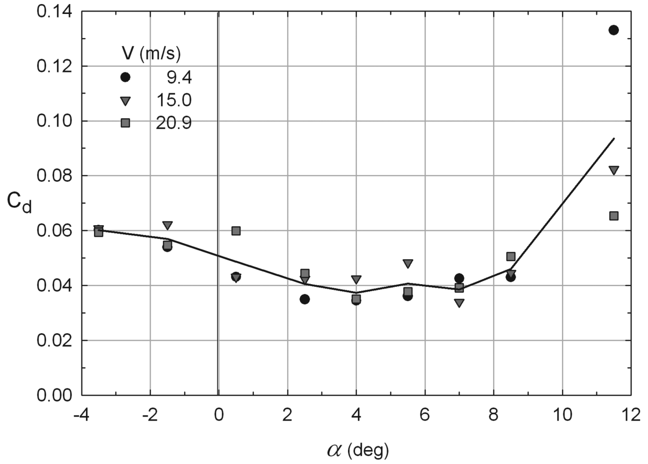

Fig. 16 Drag coefficient of the parafoil section at different freestream velocities. The solid curve indicates the average value at each angle of attack.

$\alpha = 11.5$ deg for the three different freestream velocities since the parafoil at the two higher velocities has not stalled yet.

The pitching moment coefficient, C_m, about the leading edge of the lower surface is shown in Fig. 17. The pitching moment coefficient decreases with the angle of attack and changes sign at $\alpha \approx 2.5$ deg. The Reynolds number effect on the pitching moment is less than that for the drag coefficient. The large scatter at $\alpha = 11.5$ deg is due to the various flow separation/stall stages at the three different freestream velocities.

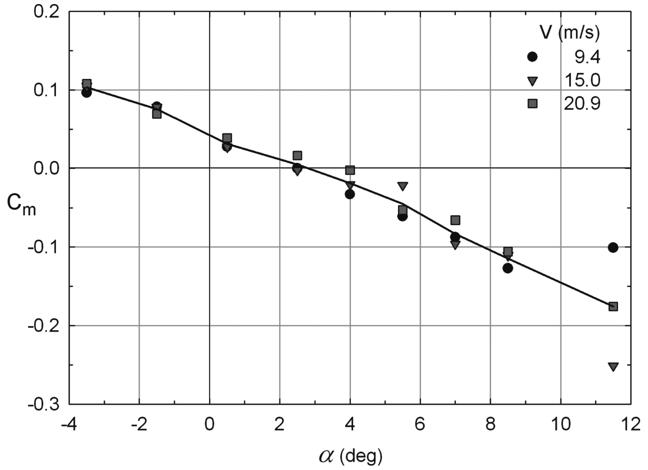

Fig. 17 Pitching moment coefficient of the parafoil section at different freestream velocities. The solid curve indicates the average value at each angle of attack.

The lift-to-drag ratio, L/D, for the parafoil section is presented in Fig. 18. There is noticeable scatter about the data after $\alpha = 2.5$ deg. For the two highest freestream velocities, the largest L/D is achieved at $\alpha = 7$ deg whereas at the lowest freestream velocity of $V_\infty = 9.4$ m/s the maximum L/D is found at $\alpha = 8.5$ deg. It is important to note that the maximum values of L/D found in the plot of Fig. 18 only refer to the specific cross section and not the entire parafoil canopy.

C. Comparison

The lift and drag coefficients of the baseline airfoil and the parafoil section are compared in this section. The lift coefficient comparison at $V_\infty = 20.9$ m/s in Fig. 19 reveals that the parafoil generates less lift than the baseline airfoil at comparable angles of attack over the range of $2.5\ \text{deg} \leq \alpha \leq 8.5$ deg. The difference can be as much as 18% less lift at $\alpha = 7$ deg even though the average lift-curve slopes are only different by 8%. Outside this range, the lift values are comparable. The decrease in lift is attributed to the flowfield modification near the cell opening. The other two freestream velocities resulted in similar behavior even though the differences in the lift coefficient were much smaller. The effect of cell opening on the lift appears to be small as the low-pressure region on the exterior of the upper surface and the higher pressure on the lower surface is maintained.

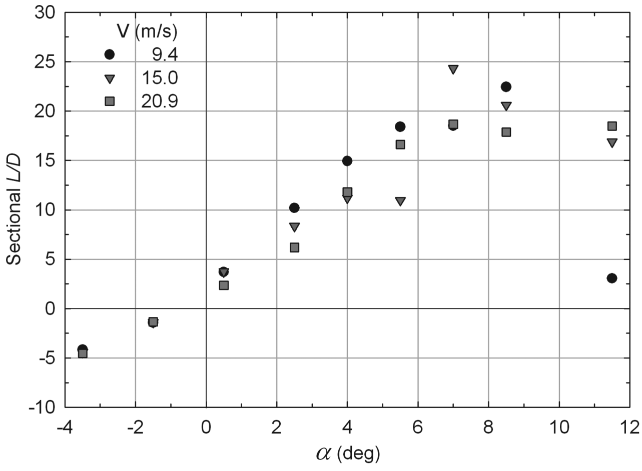

Fig. 18 Lift-to-drag ratio of the parafoil section at different freestream velocities.

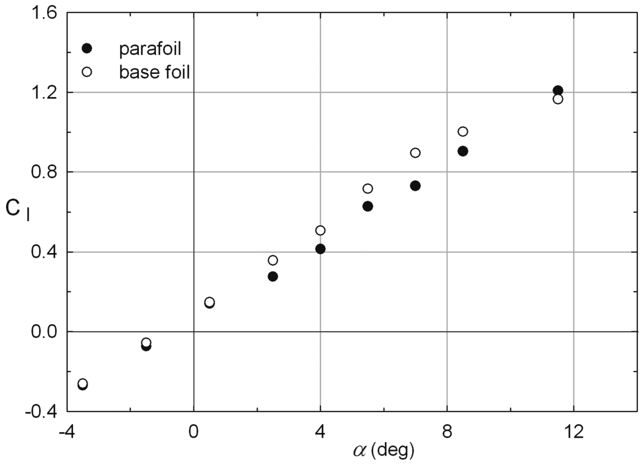

Fig. 19 Comparison of the baseline airfoil and the parafoil section lift coefficients at the highest freestream velocity.

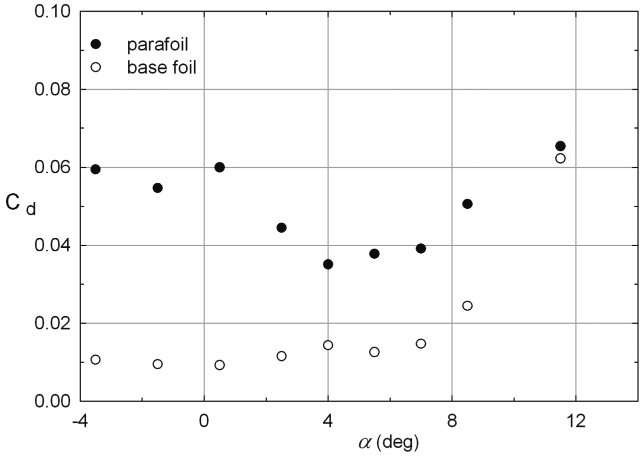

Fig. 20 Comparison of the baseline airfoil and the parafoil section drag coefficients at the highest freestream velocity.

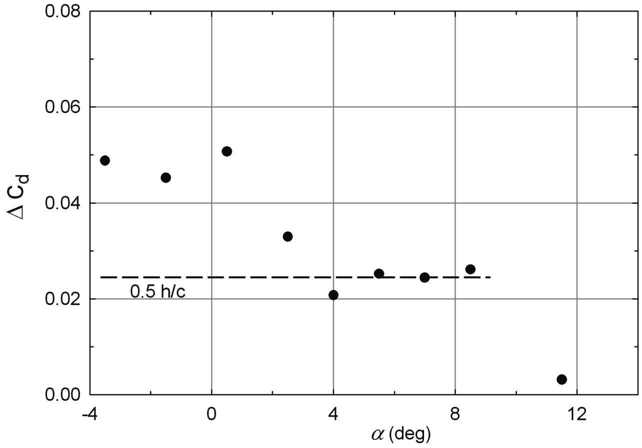

Fig. 21 Drag coefficient increase due to the parafoil cell opening at the highest freestream velocity. The dashed line shows the expression used to estimate the opening effect.

The drag coefficients at the freestream velocity of $V_\infty = 20.9\ \mathrm{m/s}$ are compared in Fig. 20. Contrary to the lift coefficient, the parafoil section has a much higher drag when compared with the baseline airfoil. For the angle-of-attack range of interest, the parafoil has a drag coefficient at least twice as much as the baseline airfoil. As the parafoil section starts to stall, the difference in the drag between the airfoil and the parafoil section decreases. The much larger drag associated with the parafoil section is attributed to the “bluff body“ created by the flow negotiating the cell opening. The vortex blocking the flow at the cell opening results in a bluff leading edge on the parafoil section as compared with the aerodynamically smooth leading edge of the baseline airfoil.

The drag coefficient difference, ΔC_d, between the parafoil section and the baseline airfoil at $V_\infty = 20.9\ \mathrm{m/s}$ is plotted in Fig. 21. The large effect caused by the cell opening geometry is clearly evident in this plot. Ideally, the drag difference should be as small as possible. Lingard [3] suggests the following engineering estimate for the effect of inlet opening, $\Delta C_d = 0.5h/c$. Here, h is the height of the cell opening and c is the section chord length. The dashed line in Fig. 21 shows this estimate for the parafoil section under study. It appears that the estimate is reasonable for 4 deg $\leq \alpha \leq$ 8.5 deg, corresponding to the expected operational range.

V. Conclusions

The flowfields about a high-performance parafoil section and the associated baseline airfoil have been computed using the CFD solver FLUENT. The Reynolds-averaged Navier–Stokes equations under the constant property, incompressible flow assumption were solved using the one equation Spalart–Allmaras turbulence model. The parafoil surfaces were assumed to be impermeable, rigid, and smooth. The computational domain and the mesh resolution were chosen to be sufficiently large and fine, respectively, so that the flowfields were independent of these parameters. The lift, drag and pitching moments of the parafoil section were calculated from the computations, and compared with the same for the baseline airfoil at three freestream velocities and a range of angles of attack. Based on the results of this investigation, the following conclusions can be drawn.

1) The parafoil flowfield consists of a vortex just inside of the cell opening, which effectively closes off the cell and diverts the flow around the leading edge. The flow about the parafoil experiences a rather bluff leading edge, in contrast to the smooth leading of the baseline airfoil. The flow pattern also creates a separation bubble on the lower leading edge of the parafoil section.

2) The lift of the parafoil section increases linearly with the angle of attack up to $\alpha = 8.5$ deg; beyond this angle stall effects appear. The lift coefficient is also nearly independent of the freestream velocity up this angle of attack. The lift-curve slope for the parafoil section is about 8% smaller than the same for the baseline airfoil. The effect of the cell opening on the lift appears to be small.

3) The parafoil cell opening has a major effect on the drag since the flow encounters a bluff leading edge. The parafoil section drag coefficient is at least twice the drag coefficient of the baseline airfoil before stall. Once the stall is approached, drag of the parafoil and the baseline airfoil become comparable. The average drag of the parafoil section is smallest over the range of 2.5 deg $\leq \alpha \leq$ 7 deg.

4) The expression $\Delta C_d = 0.5h/c$ suggested for estimating the drag increase due to the cell opening appears to provide a reasonable value over the practical range of 4 deg $\leq \alpha \leq$ 8.5 deg.

As the parafoil drag is greatly affected by the flow pattern near the cell opening, changes to the leading-edge geometry that modify the flow pattern may be quite effective in enhancing the lift-to-drag ratio and the overall performance of the parafoil canopy.

Acknowledgments

This work has been supported by the Airdrop Technology Team at Natick Soldier Systems Center under contract W911QY-08-P-0361. Assistance of Calvin Lee and Kenneth Desabrais at Natick and Justin Barber at Airborne Systems North America during various phases of this project is greatly appreciated.

References

[1] Benney, R., Barber, J., McGrath, J., McHugh, J., Noetscher, G., and Tavan, S., “The Joint Precision Airdrop System Advanced Concept Technology Demonstration,” 18th AIAA Aerodynamic Decelerator Systems Technology Conf., AIAA Paper 2005-1601, Munich, Germany, May 2005.

[2] Berland, J. C., Dunker, S., George, S., and Barber, J., “Development of a Low Cost 10,000 lb Capacity Ram-Air Parachute,” 18th AIAA Aerodynamic Decelerator Systems Technology Conf., AIAA Paper 2005-1626, Munich, Germany, May 2005.

[3] Lingard, J. S., “Precision Aerial Delivery Seminar: Ram-Air Parachute Design,” *Proceedings of the 13th AIAA Aerodynamic Decelerator Systems Technology Seminar*, AIAA, Reston, VA, 1995, pp. 1–51.

[4] Burk, S. M., and Ware, G. M., “Static Aerodynamic Characteristics of Three Ram-Air Inflated Low Aspect Ratio Wings,” NASA TN-D-4182, 1967.

[5] Nicolaides, J. D., Speelman, R. J., III, and Menard, G. L. C., “A Review of Para-foil Applications,” *Journal of Aircraft*, Vol. 7, No. 5, 1970, pp. 423–431.
doi:10.2514/3.44194

[6] Ware, G. M., and Hassell, J. L., “Wind Tunnel Investigations of Ram-Air Inflated All-Flexible Wings of Aspect ratio 1.0 to 3.0,” NASA TM-SX-1923, 1969.

[7] Tribot, J.-P., Rapuc, M., and Durand, G., “Large Gliding Parachute Experimental and Theoretical Approaches,” 14th AIAA Aerodynamic Decelerator Systems Technology Conf., AIAA Paper 97-1482, Reston, VA, 1997.

[8] Ross, J. C., “Computational Aerodynamics in the Design and Analysis

of Ram-Air-Inflated Wings," RAeS/AIAA 12th Aerodynamic Decelerator Systems Technology Conf., AIAA, Reston, VA, AIAA Paper 93-1228, 1993.

[9] Balaji, R., Mittal, S., and Rai, A. K., "Effect of Leading Edge Cut on the Aerodynamics of Ram-Air Parachutes," *International Journal for Numerical Methods in Fluids*, Vol. 47, No. 1, 2005, pp. 1–17. doi:10.1002/fld.779

[10] Mittal, S., Saxena, P., and Singh, A., "Computation of Two-Dimensional Flows Past Ram-Air Parachutes," *International Journal for Numerical Methods in Fluids*, Vol. 35, No. 6, 2001, pp. 643–667. doi:10.1002/1097-0363(20010330)35:6<643::AID-FLD107>3.0.CO;2-M

[11] Kalro, V., Aliabadi, S., Garrard, W., and Tezduyar, T., "Parallel Finite Element Simulation of Large Ram-Air Parachutes," *International Journal for Numerical Methods in Fluids*, Vol. 24, No. 12, 1997, pp. 1353–1369. doi:10.1002/(SICI)1097-0363(199706)24:12<1353::AID-FLD564>3.0.CO;2-6

[12] Tezduyar, T. E., Kalro, V., and Garrard, W., "Parallel Computational Methods for 3D Simulation of a Parafoil with Prescribed Shape Changes," *Parallel Computing*, Vol. 23, 1997, pp. 1349–1363. doi:10.1016/S0167-8191(97)00057-4

[13] Spalart, P. R., and Allmaras, S. R., "A One-Equation Turbulence Model for Aerodynamic Flows," AIAA Paper 92-0439, Jan. 1992.

[14] Selig, M., Guglielmo, J., Broeren, A., and Giguère, P., *Summary of Low-Speed Airfoil Data*, SoarTech Publications, Vol. 1, Virginia Beach, VA, 1995.

[15] Celik, I. B., Ghia, U., Roache, P. J., Freitas, C. J., Coleman, H., and Raad, P. E., "Procedure for Estimation and Reporting of Uncertainty Due to Discretization in CFD Applications," *Journal of Fluids Engineering*, Vol. 130, July 2008, Paper 078001. doi:10.1115/1.2960953